The Aeronautical Journal (2025), **129**, pp. 2648–2669
doi:10.1017/aer.2025.41

ROYAL AERONAUTICAL SOCIETY

RESEARCH ARTICLE

Linear parameter-varying model order reduction and control design of FLEXOP demonstrator aircraft

W. Gao, W. Jiang, Q. Li and B. Lu†

School of Aeronautics and Astronautics, Shanghai Jiao Tong University, Shanghai, China
Corresponding author: B. Lu; beilu@sjtu.edu.cn

Received: 27 October 2024; **Revised:** 22 January 2025; **Accepted:** 1 April 2025

Keywords: flexible aircraft; linear parameter-varying system; model order reduction; rigid-flexible coupling control

Abstract

To capture the airspeed-dependent dynamics of flexible aircraft, high-order aeroservoelastic systems can generally be expressed as linear parameter-varying (LPV) models. This paper presents a comprehensive model order reduction and control design process for grid-based LPV systems, and takes the flexible aircraft FLEXOP as an example for verification. The LPV model order reduction method is extended from projection-based linear time-invariant methods through construction of continuous transformations. The corresponding algorithm can be programmed to automatically perform the model order reduction for LPV systems and simultaneously ensure the state consistency between grid points and the continuity of state-space data interpolation. By applying this method, a 680th-order high-fidelity LPV model of the FLEXOP aircraft is reduced to a control-oriented model with only 19 states. Considering that the frequencies of rigid-body and flexible modes are close under certain parameter conditions, an integrated design approach for rigid-flexible coupling control is employed in this paper. Instead of separately designing a baseline rigid-body flight controller and a flutter suppression controller for each unstable flexible mode, a parameter-dependent dynamic output-feedback controller is designed. The resulting controller effectively expands the flutter-free flight envelope, ensuring rigid-body attitude and velocity tracking performance while stabilising the two originally unstable flutter modes.

Nomenclature

A, B, C, D	state-space matrices of the full-order model
$\bar{A}, \bar{B}_u, \bar{B}_w, \bar{C}_y, \bar{C}_z, \bar{D}_{yu}, \bar{D}_{yw}, \bar{D}_{zu}, \bar{D}_{zw}$	state-space matrices of the generalised plant
A_k, B_k, C_k, D_k	state-space matrices of the controller
A_r, B_r, C_r, D_r	state-space matrices of the reduced-order model
G_1, G_2	dynamic systems
IMU	inertial measurement unit
LPV	linear parameter-varying
LTI	linear time-invariant
$[M_k]_{i,j}$	distance metric between Π_i and Π_j for modal matching
p	roll rate
q	pitch rate
q_{l6}, q_{r6}	wingtip pitch rates
r	reference signal
$\mathbb{R}$	real space

† Author's notes

© The Author(s), 2025. Published by Cambridge University Press on behalf of Royal Aeronautical Society. This is an Open Access article, distributed under the terms of the Creative Commons Attribution licence (https://creativecommons.org/licenses/by/4.0/), which permits unrestricted re-use, distribution and reproduction, provided the original article is properly cited.
https://doi.org/10.1017/aer.2025.41 Published online by Cambridge University Press

$\mathcal{S}_1, \mathcal{S}_2, \mathcal{V}, \mathcal{W}$	vector spaces
u	input vector
V, W, V_r, W_r	transformation matrices
V_a	airspeed
w	external disturbance of the generalised plant
x, x_r	state vectors
y, $\bar{y}$, z	output vectors
W_{ideal}, W_n, W_p, W_u	weighting functions

Greek symbol

α	angle-of-attack
β	sideslip angle
γ	performance index of the controller
δ_ν	ν-gap
θ	pitch angle
ϕ	roll angle
Π, Π_i, Π_j, Π_r, Π_t, $\Pi_{V,V}$, $\Pi_{V,W}$	projection matrices
ρ	scheduling parameter
ω	angular frequency

1.0 Introduction

Advancements in material technology make it possible to manufacture lightweight, flexible, and high-strength structures, driving the research and application of flexible aircraft. The design of high-aspect-ratio flexible wings becomes a popular approach to improving aircraft energy efficiency [1]. However, flexible structures are more susceptible to deformation or vibration under gust and manoeuvering loads [2], which may couple with rigid body motion, potentially degrading flight quality and, in severe cases, compromising flight safety [3]. The promising prospects and accompanying challenges have attracted a large amount of research on flexible aircraft, with typical projects including the X56-A in the United States [4, 5], and the Flutter Free FLight Envelope eXpansion for ecOnomic Performance improvement (FLEXOP) [6] and Flight Phase Adaptive Aero-Servo-Elastic Aircraft Design Methods (FLiPASED) projects in the European Union [7]. The former is a flying wing configuration, the latter two are conventional aircraft configurations, and all aim to develop and test active flutter suppression algorithms. To achieve this goal, one of the key challenges in flexible aircraft research is rigid-flexible coupling dynamics modeling and control design [8].

Based on existing modeling methods that are well-suited for engineering applications [9, 10], the complexity of rigid-flexible coupling dynamics modeling primarily arises from its interdisciplinary integration and the need for updates with experimental data [11]. Due to the inclusion of unsteady aerodynamics and structural dynamics, flexible aircraft models typically exhibit nonlinear and high-order characteristics. Considering the variation of dynamic characteristics across the entire flight envelope, the linear parameter-varying (LPV) modeling approach is commonly employed for flexible aircraft [12]. By interpolating the linear time-invariant (LTI) models derived under a family of flight conditions, a grid-based LPV model can be obtained as an approximation for the aircraft dynamics within a specific parameter range [13]. The LPV model has the same order as the nonlinear model, and thus the model order reduction is a necessary step before the subsequent controller design. In the previous studies of FLEXOP, constrained by the LPV model order reduction techniques at that time [14], a bottom-up approach is applied to first reduce the order of structural dynamics and aerodynamics subsystems and then combine them with other subsystems to get the integrated model [6, 15]. The resulting grid-based LPV model contains 56 state variables, leaving potential room for further reduction and making it more suitable for LPV controller design [16, 17]. This paper will take this 56th-order FLEXOP model in the LPV form as a comparison [18], and focus on the acquisition of a lower order control-oriented model as well as design for rigid-body control and active flutter suppression.

https://doi.org/10.1017/aer.2025.41 Published online by Cambridge University Press

The most intuitive strategy for LPV model reduction is to extend the techniques used for LTI systems to LPV models. It is important to note that although low-order LTI models can be obtained at each grid point using LTI model order reduction, there is no guarantee that a continuous low-order LPV model can be constructed by interpolating these models. Taking modal truncation as an example, differences in dynamics of local models at various grid points may lead to inconsistencies in retained states and their order. To address this issue, a modal matching algorithm is proposed by using a distance metric based on eigenvalues [19]. It matches the same modes across different grid points one-to-one and arranges the modal vectors to obtain modal truncation with retaining the same states in a consistent sequence. However, if the system has repeated eigenvalues or intersecting eigenvalue trajectories, the matching algorithm may struggle to distinguish the related modes, which limits its applicability. Balanced truncation retains states based on their input-output contribution, making it well-suited for control-oriented model order reduction. But similar state inconsistency issues can also arise when applied to LPV systems. Several approaches have been explored for obtaining continuous balanced LPV reduced-order models, such as finding balancing transformations by directly solving linear matrix inequalities [20, 21], adopting common bases for deriving consistency transformations [22], constructing continuous transformations based on oblique projection approximation [23], and using genetic algorithms to automatically determine physical states for minimising the trial-and-error process [24]. However, they tend to suffer from accuracy issues, either due to approximations or as a result of weak consistency. Inspired by these studies, particularly the approach involving oblique projection approximation, a method is developed that constructs a modal matching metric and continuous transformations based on oblique projections, achieving significant order reduction for flexible aircraft models [25, 26]. This paper will attempt to apply this method to reduce the number of states of the FLEXOP model.

A low-order LPV model alleviates the constraints of computational resources on controller design and implementation. This allows for a broader range of controller design methods to be considered [27, 28]. Given the large variations in model dynamics during flight, different nonlinear control methods, such as nonlinear model predictive control [29], adaptive control [30] and nonlinear dynamic inversion [31], have been explored to ensure performance across the entire flight envelope [32]. Due to its ability to directly design the controller based on the LPV model, LPV control has also been applied in some cases [33]. This approach simplifies control design by utilising linear control techniques while accommodating parameter variations, ensuring robust performance throughout the flight envelope. Its flexibility and effectiveness in handling large dynamic changes make it a preferred choice in modern control applications for flexible aircraft. This method is initially applied to the flutter control of a cantilever flexible wing section [34], and later extended to control the entire flexible aircraft called mini Multi Utility Technology Testbed (MUTT) of the University of Minnesota [35]. In the well-known NASA X-56A project, it has been attempted for controlling body freedom flutter [36]. In the FLEXOP project, the LPV method has also been employed for independent control design for each flutter mode, successfully increasing the critical flutter velocity [17, 37]. However, we found that the closed-loop critical flutter velocity can be further improved by directly utilising the multi-objective optimisation capabilities of LPV control for integrated flutter suppression and attitude control.

The FLEXOP project has provided extensive and valuable engineering experience, practical insights, and data for the modeling and control of flexible aircraft. Building upon these foundations, this paper will present a comprehensive process for LPV model order reduction and LPV controller design tailored to flexible aircraft, with the FLEXOP aircraft serving as an illustrative example. From practical aspects, the main contributions of this paper are as follows:

1. A detailed theoretical derivation and implementation process of the projection-based LPV model order reduction method is provided. The order of the FLEXOP demonstrator model is further reduced using this method.
2. A dynamic output-feedback LPV controller is designed using the reduced-order model with the rigid-flexible coupling effects considered. The flutter-free flight envelope of the FLEXOP demonstrator is effectively expanded.

https://doi.org/10.1017/aer.2025.41 Published online by Cambridge University Press

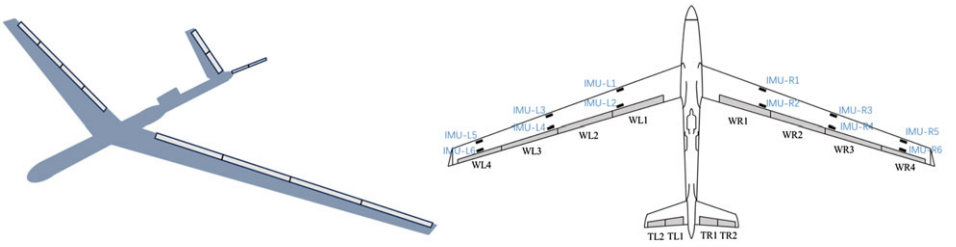


Figure 1. *The sketch of FLEXOP.*

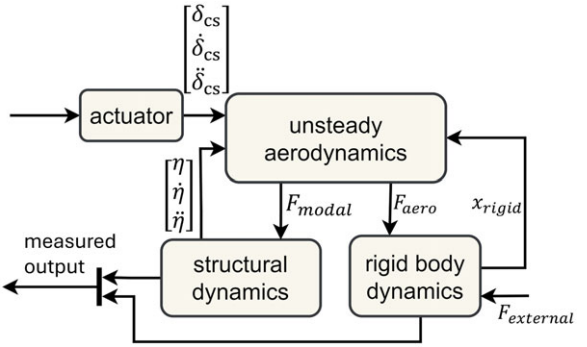


Figure 2. *The integration of subsystems for rigid-flexible coupled dynamics modeling.*

The remainder of this paper is organised as follows: Section 2.0 gives a brief description of the FLEXOP demonstrator model. In Section 3.0, the theoretical background and algorithm implementation of the LPV model order reduction technique are provided. In Section 4.0, the algorithm is applied to reduce the order of the FLEXOP model. In Section 5.0, the LPV control problem is formulated for rigid-body attitude control and flutter suppression. Closed-loop simulations are conducted to demonstrate the effectiveness of the controller. The paper concludes in Section 6.0.

2.0 Brief description of the model

The model used in this paper is the demonstrator aircraft from the FLEXOP project [6], whose basic configuration is shown in Fig. 1. It is a flexible drone with a wingspan of 7 m and aspect ratio of 20, powered by an engine mounted on the fuselage, with a takeoff weight ranging from 55 to 66 kg. There are eight control surfaces on the main wing and four control surfaces on the V-tail, symmetrically arranged on both sides. The innermost WL1 and WR1 are used as lift augmentation devices, WL2 and WL3 as well as WR2 and WR3 function as ailerons. The control surfaces on the V-tail, through symmetrical and asymmetrical deflections, provide the functions of the elevator and rudder. The outermost WL4 and WR4 are independently used for flutter control. In addition to the sensing devices used in the rigid aircraft, a total of 12 inertial measurement units (IMUs) are installed on both sides of the main wing to provide information of the flexible vibration for flutter suppression control.

The rigid-flexible coupled dynamics modeling framework of the aircraft is shown in Fig. 2. The aerodynamic model is obtained through the vortex lattice method and doublet lattice method, and supplemented by computational fluid dynamics methods. The structural model is built based on finite element method and updated through experiments. The rigid-flexible coupling is achieved through the mean-axes method, and the detailed modeling and updating process is given in the literature [18]. The order of the high-fidelity model (the 4.0 release model development by DLR-SR) of the aircraft is 680, including 100 structural states, 544 aerodynamic states, 12 rigid body states and 24 actuator states.

Due to the coupling effects between rigid body motion, flexible deformation and unsteady aerodynamics, the dynamic characteristics of the aircraft change significantly with flight speed. For dynamic

https://doi.org/10.1017/aer.2025.41 Published online by Cambridge University Press

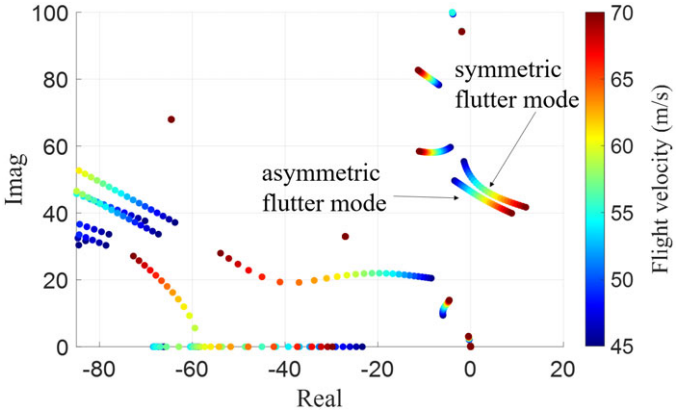


Figure 3. *Pole migration of the high-fidelity model.*

analysis and controller synthesis, it is often represented in the form of an LPV model. By choosing 26 velocity points from 45 m/s to 70 m/s at intervals of 1 m/s and performing linearisation, a grid-based LPV model with flight velocity as the scheduling parameter is derived.

$$\begin{aligned} \dot{x} &= A(\rho)\, x + B(\rho)\, u \\ y &= C(\rho)\, x + D(\rho)\, u \end{aligned} \tag{1}$$

where $x \in \mathbb{R}^{n_x}$ is the state, $u \in \mathbb{R}^{n_u}$ is the input, $y \in \mathbb{R}^{n_y}$ is the measurement, $A(\rho) \in \mathbb{R}^{n_x \times n_x}$, $B(\rho) \in \mathbb{R}^{n_x \times n_u}$, $C(\rho) \in \mathbb{R}^{n_y \times n_x}$ and $D(\rho) \in \mathbb{R}^{n_y \times n_u}$ are parameter-dependent system matrices. Their values at any given ρ can be obtained through interpolation of system matrices at ρ_k, where ρ is the scheduling parameter (i.e., the airspeed in this case), with the subscript k indicating different parameter values (also called grid points or operating points).

The pole migration of the model in the relatively low-to-mid frequency range is shown in Fig. 3, where only the poles with nonnegative imaginary part are presented due to the symmetry property of complex conjugate pairs. As the velocity increases, two flexible modes gradually become unstable. The corresponding critical flutter velocities are approximately 52 m/s and 55 m/s, with frequencies of 50 rad/s and 46 rad/s, respectively.

Considering that such a high-order model is difficult to use in controller design, a bottom-up modeling approach is adopted in previous studies to simplify the model. By truncating the aerodynamic states and structural modes separately before integrating the model, the model order can be reduced to 56 [6]. For grid-based LPV systems, it is often to consider all grid points within the selected parameter space to design the LPV controllers. If choosing dynamic output-feedback control, the order of the controller is determined by the order of the open-loop plant, which also affects the size of the optimisation problem when solving for the controller. From the perspective of practical application, the order of the FLEXOP model obtained using the bottom-up modeling approach is still relatively high. In the following section, the oblique projection-based LPV model order reduction method will be applied and the order of the FLEXOP model will be further reduced with state consistency ensured.

3.0 LPV model order reduction

This section will start with an introduction to the basic concept of projection, followed by the description of projection-based model order reduction methods, with an emphasis on how to extend LTI methods to LPV systems. The corresponding LPV model order reduction algorithm is given and the implementation process is explained in detail. Based on this method, further model order reduction for the FLEXOP is performed.

https://doi.org/10.1017/aer.2025.41 Published online by Cambridge University Press

3.1 Basic concept of projection

As described in Section 2.0, the flexible aircraft can be represented as a grid-based LPV model of the form given in Equation (1). If traditional LTI model order reduction methods are independently applied at each grid point, the local transformation matrices will be selected separately. This may result in inconsistencies in the preserved states or their order among different grid points [23]. Here, the concept of oblique projection is introduced to avoid this issue [38].

Definition 1. *A matrix $\Pi \in \mathbb{R}^{n\times n}$ is a projection matrix (or idempotent matrix) of a real value vector space $\mathbb{R}^n$ if*

$$\Pi^2 = \Pi \tag{2}$$

Denoting Im $(\Pi) = \mathcal{S}_1$ and Ker $(\Pi) = \mathcal{S}_2$, Π defines the projection onto $\mathcal{S}_1$ along $\mathcal{S}_2$, where Im $(\cdot)$ indicates the imagine space and Ker $(\cdot)$ represents the null space. The real value vector space $\mathbb{R}^n$ can be decomposed as the direct sum of the imagine space and null space of the projection matrix.

$$\mathbb{R}^n = \mathcal{S}_1 \oplus \mathcal{S}_2 \tag{3}$$

When $\mathcal{S}_2 = \mathcal{S}_1^{\perp}$, the projection in Equation (2) is an orthogonal projection and can be expressed as

$$\Pi_{V,V} = VV^{\mathrm{T}} \tag{4}$$

where $(\cdot)^{\perp}$ denotes orthogonal complement, $V \in \mathbb{R}^{n\times r}$ is an orthogonal matrix whose columns span $\mathcal{S}_1$. For the general case where $\mathcal{S}_2$ may be distinct from $\mathcal{S}_1^{\perp}$, the projection is an oblique projection and can be expressed as

$$\Pi_{V,W} = V(W^{\mathrm{T}}V)^{-1}W^{\mathrm{T}} \tag{5}$$

where $V \in \mathbb{R}^{n\times r}$ and $W \in \mathbb{R}^{n\times r}$ are two full-column rank matrices whose columns span respectively $\mathcal{S}_1$ and $\mathcal{S}_2$.

Based on the above definition of projections, several important corollaries are given below and will be used in the projection-based LPV model order reduction.

Corollary 1. *If matrices $V \in \mathbb{R}^{n_f\times n_r}$ and $W \in \mathbb{R}^{n_f\times n_r}$ satisfy $W^TV = I_{n_r}$, then $\left(VW^T\right)\left(VW^T\right) = V\left(W^TV\right)W^T = VW^T$ holds. According to Definition 1, $VW^T \in \mathbb{R}^{n_f\times n_f}$ is a projection matrix.*

Corollary 2. *Given projection matrices Π_{V_i,W_i} and Π_{V_j,W_j}, if Im $(V_i) \cap$ Im $\left(V_j\right) = 0$, Im $(W_i) \cap$ Im $\left(W_j\right) = 0$, Im $(V) \perp$Im $\left(W_j\right)$ and Im $(W_i) \perp$Im $\left(V_j\right)$ are satisfied, then $\Pi_{V_i,W_i} + \Pi_{V_j,W_j}$ is also a projection matrix with Im $(V) =$ Im $(V_i) \oplus$ Im $\left(V_j\right)$ and Im $(W) =$ Im $(W_i) \oplus$ Im $\left(W_j\right)$.*

3.2 Projection-based method

For a high order model as shown in Equation (1), based on the projection $\Pi_{V(\rho),W(\rho)}$, the model order reduction can be started from approximating x as $V(\rho)\, x_r$.

$$\frac{d\left(V(\rho)\, x_r\right)}{dt} = A(\rho)\, V(\rho)\, x_r + B(\rho)\, u + r(t) \tag{6}$$

where $x \in \mathbb{R}^{n_f}$ and $x_r \in \mathbb{R}^{n_r}$ with $n_r < n_f$. $V(\rho) \in \mathbb{R}^{n_f\times n_r}$ and the related subspace $\mathcal{V}$ spanned by it is called basis space. $r(t)$ is the residual introduced by the approximation. Constrain the residual to be orthogonal to a subspace $\mathcal{W}$ defined by a test basis $W(\rho) \in \mathbb{R}^{n_f\times n_r}$ as $W(\rho)^{\mathrm{T}}r(t) = 0$. This leads to the governing equation of the Petrov-Galerkin projection model order reduction [39]. Considering the LTI model at a fixed grid point ρ_k, and $V(\rho_k)$ and $W(\rho_k)$ are constant matrices with rank $\left(W^{\mathrm{T}}(\rho_k)\, V(\rho_k)\right) = n_r$, and there is

$$W^{\mathrm{T}}(\rho_k)\, V(\rho_k)\, \dot{x}_r = W^{\mathrm{T}}(\rho_k)\left(A(\rho_k)\, V(\rho_k)\, x_r + B(\rho_k)\, u\right) \tag{7}$$

https://doi.org/10.1017/aer.2025.41 Published online by Cambridge University Press

The high-dimensional state x can be projected to the reduced-order state by $x_r = (W^{\mathrm{T}}(\rho_k)\, V(\rho_k))^{-1} W^{\mathrm{T}}(\rho_k)\, x$ as

$$\begin{aligned} \dot{x}_r &= A_r(\rho_k)\, x_r + B_r(\rho_k)\, u \\ y_r &= C_r(\rho_k)\, x_r + D_r(\rho_k)\, u \end{aligned} \tag{8}$$

where

$$\begin{aligned} A_r(\rho_k) &= (W^{\mathrm{T}}(\rho_k)\, V(\rho_k))^{-1} W^{\mathrm{T}}(\rho_k)\, A(\rho_k)\, V(\rho_k) \in \mathbb{R}^{n_r \times n_r} \\ B_r(\rho_k) &= (W^{\mathrm{T}}(\rho_k)\, V(\rho_k))^{-1} W^{\mathrm{T}}(\rho_k)\, B(\rho_k) \in \mathbb{R}^{n_r \times n_u} \\ C_r(\rho_k) &= C(\rho_k)\, V(\rho_k) \in \mathbb{R}^{n_y \times n_r} \\ D_r(\rho_k) &= D(\rho_k) \in \mathbb{R}^{n_y \times n_u} \end{aligned} \tag{9}$$

The original system can be reconstructed by $\tilde{x} = V(\rho_k)\, x_r$. Pre-multiplying the state equation in Equation (8) by $V(\rho_k)$, the following equivalent system is obtained.

$$\begin{aligned} \dot{\tilde{x}} &= \Pi_{V(\rho_k),W(\rho_k)} (A(\rho_k)\, \tilde{x} + B(\rho_k)\, u) \\ \tilde{y} &= C(\rho_k)\, \tilde{x} + D(\rho_k)\, u \end{aligned} \tag{10}$$

Remark 1. Equation (10) *indicates that as long as the subspaces $\mathcal{V}$ and $\mathcal{W}$ remains unchanged, the choice of bases V and W does not affect the reconstruction of the original states. Given a high-order dynamic system, a corresponding projection-based reduced-order model is uniquely defined by its associated Petrov-Galerkin projector $\Pi_{V(\rho_k),W(\rho_k)}$, and this projector is uniquely defined by the two subspaces $\mathcal{V} = Im(V)$ and $\mathcal{W} = Im(W)$.*

Model order reduction techniques for LTI systems such as balanced truncation and proper orthogonal decomposition both fall under the category of Petrov-Galerkin projection-based methods. If $\mathcal{W} = \mathcal{V}$, the related method is called a Galerkin projection method and modal truncation belongs to this category.

Remark 2. *Assume that $T = [V_r, V_t]$ and $T^{-1} = [W_r, W_t]^T$ are the eigenvector matrices of the system matrix A and its inverse, respectively. By selecting $V = V_r$ and $W = W_r$ as the basis and test basis to obtain the reduced-order model in Equation (8), the corresponding model order reduction method is referred to as modal truncation.*

Remark 3. *If $T = [V_r, V_t]$ and $T^{-1} = [W_r, W_t]^T$ are constructed based on singular value decomposition of the product of controllability Gramian W_c and observability Gramian W_o of the system*

$$W_{\mathrm{c}} W_{\mathrm{o}} T = T \Sigma^2 \tag{11}$$

where Σ is a diagonal matrix and the entries on the diagonal are known as Hankel singular values. The transformation $x = Tx_r$ provides a system with states hierarchically ranked according to their ability to capture the input-output characteristics [40]. In this case, select $V = V_r$ and $W = W_r$, and then the related model order reduction method is balanced truncation. The details for constructing W_{c} and W_{o} are described in the literature [41].

Now considering the LPV model for the whole parameter space, the basis $V(\rho)$ and test basis $W(\rho)$ are parameter-dependent matrices. Still approximate x as $V(\rho)\, x_r$ and there is

$$\frac{d(V(\rho)\, x_r)}{dt} = V(\rho)\, \dot{x}_r + \sum_{i=1}^{n_\rho} \frac{\partial V(\rho)}{\partial \rho_i} \dot{\rho}_i x_r \tag{12}$$

where n_ρ is the number of scheduling parameters. Then Equation (6) becomes

$$V(\rho)\, \dot{x}_r = \left(-\sum_{i=1}^{n_\rho} \frac{\partial V(\rho)}{\partial \rho_i} \dot{\rho}_i + A(\rho)\, V(\rho) \right) x_r + B(\rho)\, u + r(t) \tag{13}$$

https://doi.org/10.1017/aer.2025.41 Published online by Cambridge University Press

Thus, the system matrix $A_r(\rho_k)$ in Equation (9) will include a term containing parameter change rates and can be expressed as

$$A_r(\rho) = (W^{\mathrm{T}}(\rho) V(\rho))^{-1} W^{\mathrm{T}}(\rho) \left(A(\rho) V(\rho) - \sum_{i=1}^{n_\rho} \frac{\partial V(\rho)}{\partial \rho_i} \dot{\rho}_i \right) \in \mathbb{R}^{n_r \times n_r} \tag{14}$$

Other system matrices $B_r(\rho)$, $C_r(\rho)$ and $D_r(\rho)$ have similar expressions as those given in Equation (9), just replacing ρ_k with ρ. It is noted when extending the projection-based LTI reduction methods to grid-based LPV models, two key issues need to be addressed: firstly, how to obtain a basis V that allows for continuous interpolation, and secondly, how to minimise the impact of parameter variation rates on the error caused by model order reduction. These two issues will be discussed in the next subsection.

3.3 LPV model order reduction algorithm

In practice, although the basis $V(\rho_k)$ obtained from LTI model reduction at discrete grid points may not be directly applicable for continuous interpolation, a new basis $V(\rho)$ suitable for continuous interpolation can be reconstructed using the oblique projection operator. Additionally, the error introduced by parameter variation can be mitigated by incorporating constraints during the reconstruction process.

Take the modal decomposition as an example. According to Remark 2, the eigenvector matrix and its inverse can be expressed in component form as

$$\begin{aligned} T(\rho) &= \left[v_1(\rho), v_2(\rho), \cdots, v_{n_f}(\rho) \right] \\ T^{-1}(\rho) &= \left[w_1(\rho), w_2(\rho), \cdots, w_{n_f}(\rho) \right]^{\mathrm{T}} \end{aligned} \tag{15}$$

According to Corollary 1, the expression $v_i(\rho) w_i^{\mathrm{T}}(\rho)$ in the modal decomposition is actually a continuous oblique projection function, denoted as $\Pi_i(\rho)$. Therefore,

$$A(\rho) = \sum_{i=1}^{n_f} \lambda_i(\rho) v_i(\rho) w_i^{\mathrm{T}}(\rho) = \sum_{i=1}^{n_f} \lambda_i(\rho) \Pi_i(\rho) \tag{16}$$

For any two component vectors in Equation (15) at grid point ρ_k, considering the sum of the oblique projection matrices formed by each of them, we have

$$\Pi_i(\rho_k) + \Pi_j(\rho_k) = v_i(\rho_k) w_i^{\mathrm{T}}(\rho_k) + v_j(\rho_k) w_j^{\mathrm{T}}(\rho_k) = \left[v_i(\rho_k), v_j(\rho_k) \right] X \cdot X^{-1} \left[w_i(\rho_k), w_j(\rho_k) \right]^{\mathrm{T}} \tag{17}$$

where matrix X represents an arbitrary invertible linear transformation of vectors $v_i(\rho_k)$ and $v_j(\rho_k)$. According to Corollary 2, $\Pi_i(\rho_k) + \Pi_j(\rho_k)$ is a uniquely defined oblique projection matrix and its subspaces will not change with the transformation X. This property can be generalised to the sum of oblique projection matrices constructed from any number of component vectors. Therefore, the local oblique projection matrix formed by $V(\rho_k)$ can be expressed as follows.

$$\Pi(\rho_k) = \sum_{i=1}^{n_f} \Pi_i(\rho_k) = \sum_{i=1}^{n_r} \Pi_i(\rho_k) + \sum_{i=n_r+1}^{n_f} \Pi_i(\rho_k) = \Pi_r(\rho_k) + \Pi_t(\rho_k) \tag{18}$$

As long as the partition of $\Pi(\rho_k)$ into $\Pi_r(\rho_k)$ and $\Pi_t(\rho_k)$ remains consistent at each grid point, a continuous oblique projection matrix function $\Pi_r(\rho)$ can be derived by interpolating $\Pi_r(\rho_k)$ at all grid points.

The partition of oblique projection matrices can be achieved by modal matching. This involves grouping the same modes at different grid points and further dividing them into two categories based on whether they are retained or truncated. Distinguishing the same modes (and the related projection matrices) at different grid points is realised through the metric proposed in Ref. (25).

$$[M_k]_{ij} = \frac{\left| \Pi_i(\rho_k) \Pi_j(\rho_{k+1}) \Pi_i(\rho_k) \right|}{\left| \Pi_i(\rho_k) \right|} \tag{19}$$

https://doi.org/10.1017/aer.2025.41 Published online by Cambridge University Press

Denoting $\Pi_j(\rho_{k+1}) = \left(v_j(\rho_k) + \Delta v\right)\left(w_j(\rho_k) + \Delta w\right)^{\mathrm{T}}$, the metric can be rewritten as

$$[M_k]_{i,j} = \left(\delta_{i,j}^2 - \delta_{i,j}\Delta w^{\mathrm{T}}\Delta v + w_i^{\mathrm{T}}(\rho_k)\,\Delta v\Delta w^{\mathrm{T}} v_i(\rho_k)\right) \tag{20}$$

where $\delta_{i,j} = w_i^{\mathrm{T}}(\rho_k)\, v_j(\rho_k)$ is the Kronecker delta that is defined based on the orthogonality condition of the eigenvectors. If the grid points of the LPV model are sufficiently dense, the last two terms in the above equation are both negligible higher-order infinitesimals, and the metric $[M_k]_{i,j}$ should approach the value of $\delta_{i,j}$ very closely. Thus, the following conditions can be used to determine whether the oblique projection matrix of two adjacent grid points should be matched to the same group.

$$\begin{cases} \text{if} [M]_{i,j} - 1 < tol, \;\; \Pi_i(\rho_k) \,\text{and}\, \Pi_j(\rho_{k+1}) \,\text{match}, \\ \text{else if} [M_k]_{i,j} < tol, \;\; \Pi_i(\rho_k) \,\text{and}\, \Pi_j(\rho_{k+1}) \,\text{donotmatch}, \\ \text{else}, \;\; \text{thedistancebetween}\rho_k \text{and}\rho_{k+1} \text{istoolarge}. \end{cases} \tag{21}$$

where *tol* is the tolerance set by considering the higher order terms in Equation (19). After completing the matching process, the oblique projection matrices can be further classified based on the requirements for retaining or truncating specific modes, and $\Pi_r(\rho_k)$ can be constructed by referring to Equation (18).

Remark 4. *For some systems, there may be cases of intersecting eigenvalue trajectories or repeated eigenvalues. In such situations, distance-based matching might result in one-to-many or many-to-many correspondences, where* $\Pi_i(\rho_k)$ *can match with multiple instances of* $\Pi_j(\rho_k)$ *when j takes different values. In this case, no further distinction is necessary. It is sufficient to ensure that these oblique projection operators, which have multiple corresponding relationships, are grouped together into* $\Pi_r(\rho_k)$ *or* $\Pi_t(\rho_k)$*, and then either truncated or retained accordingly.*

Then, $\Pi_r(\rho_k)$ can be used to formulate a continuous transformation to achieve LPV model order reduction by multiplying with a continuous matrix function $V_0(\rho)$.

$$\begin{aligned} V_r(\rho) &= \Pi_r(\rho)\, V_0(\rho) \\ W_r(\rho) &= \Pi_r^{\mathrm{T}}(\rho)\, V_r(\rho)\left(V_r^{\mathrm{T}}(\rho)\, V_r(\rho)\right)^{-1} \end{aligned} \tag{22}$$

Thus, the reduced-order LPV model with state consistency can be obtained by substituting $V_r(\rho_k)$ and $W_r(\rho_k)$ into V and W respectively in Equation (9) at each grid point ρ_k. The selection of the matrix function $V_0(\rho)$ should ensure that the matrix function $\Pi_r(\rho)\, V_0(\rho)$ has the same column rank as $\Pi_r(\rho)$, so that the image space spanned by $V_r(\rho)$ is equal to the one spanned by $V_0(\rho)$. In general, a constant basis can be used for generating V_0.

$$\begin{aligned} U\Sigma N^{\mathrm{T}} &= \mathrm{svd}\left(\Pi_r(\rho_1), \Pi_r(\rho_2), \cdots, \Pi_r\left(\rho_{n_k}\right)\right) \\ V_0(\rho_k) &\equiv U_r = U(:, 1{:}\, n_r) \end{aligned} \tag{23}$$

where $\mathrm{svd}(\cdot)$ denotes the singular value decomposition. This procedure can be generalised to multi-dimensional LPV parameters spaces. For systems with slowly varying parameters, the parameter variation rate is negligible and the related term in Equation (14) may not be taken into account.

In this paper, the scheduling parameter ρ is the airspeed, and thus the parameter space is one-dimensional, allowing for further derivation of a parameter-dependent matrix function V_0. Assuming V_0 is already the desired V_r, substituting it into Equation (22) and differentiating the equation yields

$$\frac{\partial \Pi_r(\rho)}{\partial \rho} V_r(\rho) = \left(I - \Pi_r(\rho)\right)\frac{\partial V_r(\rho)}{\partial \rho} \tag{24}$$

Since $\Pi_r(\rho)$ is already obtained, the above equation is a differential equation with respect to V_r. The solution to this equation is not unique as $\mathrm{rank}\left(I - \Pi_r(\rho)\right) < n_f$. Thus, the following constraint is introduced.

$$\Pi_r(\rho)\frac{\partial V_r(\rho)}{\partial \rho} = 0 \tag{25}$$

Pre-multiplying W_r^{T} to both sides of the above equation yields

$$W_r^{\mathrm{T}}(\rho)\,\Pi_r(\rho)\,\tfrac{\partial V_r(\rho)}{\partial \rho} = W_r^{\mathrm{T}}(\rho)\, V_r(\rho)\, W_r^{\mathrm{T}}(\rho)\,\tfrac{\partial V_r(\rho)}{\partial \rho} = W_r^{\mathrm{T}}(\rho)\,\tfrac{\partial V_r(\rho)}{\partial \rho} = 0 \tag{26}$$

https://doi.org/10.1017/aer.2025.41 Published online by Cambridge University Press

Algorithm 1 Oblique projection-based LPV model order reduction

Require: The full-order LPV model (as Equation (1)); The order to be retained n_r

1: Calculate the number of grid points n_k
2: **for all** $i = 1$ to n_f and $k = 1$ to n_k **do**
3: Construct projection matrices $\Pi_i(\rho_k) = v_i(\rho_k)\, w_i^{\mathrm{T}}(\rho_k)$
4: **end for**
5: **for all** $k = 1$ to $n_k - 1$, $i = 1$ to n_f and $j = 1$ to n_f **do**
6: Calculate the metric $[M_k]_{i,j}$ (Equation (19))
7: **end for**
8: Group the oblique projection matrices (Equation (21))
9: **for** $k = 1$ to n_k **do**
10: Divide the groups into two categories of 'retain' and 'truncate', calculate $\Pi_r(\rho_k)$ (Equation (18))
11: **end for**
12: Calculate the constant transformation V_0 (Equation (23))
13: **for** $k = 1$ to n_k **do**
14: Calculate the transformations $V_r(\rho_k)$ and $W_r(\rho_k)$ (Equation (22) and (29))
15: Calculate $A_r(\rho_k)$, $B_r(\rho_k)$,$C_r(\rho_k)$, $D_r(\rho_k)$ (Equation (9))
16: **end for**
17: **return** A reduced-order model (as Equation (8))

In addition to making the equation solvable, this constraint also eliminates terms related to $\dot{\rho}$ in Equation (14). Substituting Equation (25) into Equation (24) yields

$$\frac{\partial \Pi_r(\rho)}{\partial \rho} V_r(\rho) = \frac{\partial V_r(\rho)}{\partial \rho} \tag{27}$$

Using finite differences to approximate differentiation at point $\rho = \rho_k$, we have

$$\begin{aligned} \left.\frac{\partial \Pi_r(\rho)}{\partial \rho}\right|_{\rho_k} &\approx \frac{\Pi_r(\rho_{k+1}) - \Pi_r(\rho_k)}{\rho_{k+1} - \rho_k} \\ \left.\frac{\partial V_r(\rho)}{\partial \rho}\right|_{\rho_k} &\approx \frac{V_r(\rho_{k+1}) - V_r(\rho_k)}{\rho_{k+1} - \rho_k} \end{aligned} \tag{28}$$

Substituting above equations into Equation (27) and solving it provide the construction method for the continuous transformation matrix as follows.

$$V_r(\rho_{k+1}) = \Pi_r(\rho_{k+1})\, V_r(\rho_k) \tag{29}$$

At point $k = 1$, $V_r(\rho_1)$ can be derived based on Equation (23). The transformations $V_r(\rho_k)$ and $W_r(\rho_k)$ at all grid points can be derived by combining Equations (22) and (29), and substituting $\Pi_r(\rho_k)$ into this combination. Then the reduced-order model can be generated according to Equation (9). In summary, the projection-based model order reduction method can be outlined as Algorithm 1.

Remark 5. *The different constructions of projection matrix $\Pi_i(\rho_k)$ in the third line of Algorithm 1 correspond to different model order reduction methods. For example, when constructed according to the eigenvectors as shown in Equation (16), the corresponding method is the modal truncation. If constructed according to the decomposition in Equation (11), the corresponding method is balanced truncation. Regardless of the method applied, as long as the original LPV model and the order to be retained are provided, the algorithm can automatically generate the reduced-order model with consistent states.*

https://doi.org/10.1017/aer.2025.41 Published online by Cambridge University Press

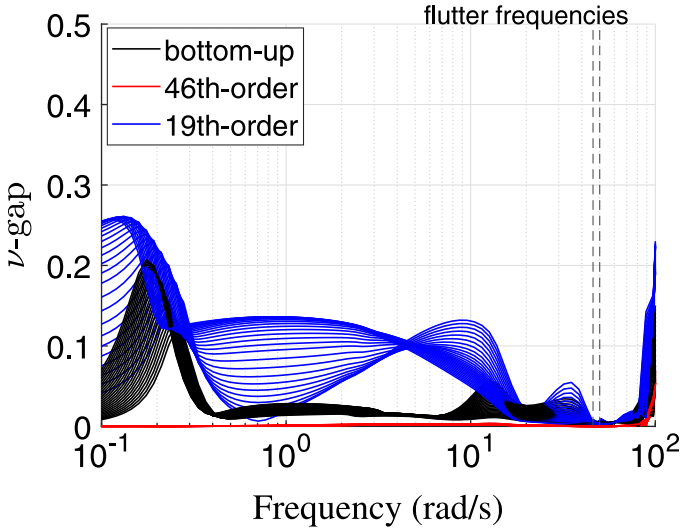


Figure 4. *ν-gap between the high-fidelity model and reduced-order models.*

4.0 Model order reduction of flexop

Following the steps outlined in the previous section, the order of the high-fidelity LPV FLEXOP model can be reduced using modal truncation and balanced truncation methods.

4.1 Main process

Assuming that high-frequency modes, which are stable and exceed the bandwidth of the aircraft, have a negligible impact on aircraft dynamics, these modes are truncated using the modal truncation method to derive an intermediate model with 46 states from the 680th-order high-fidelity model. Then, by focusing on preserving the input-output characteristics, the model is further reduced using balanced truncation, ultimately resulting in a model with only 19 states. The final retained order is determined with reference to the ν-gap criterion, keeping it close to zero within the frequency range of [0,100] rad/s. This guarantees that the controller designed for reduced-order model can also achieve similar performance when applied to the high-fidelity model. The ν-gap between systems G_1 and G_2 is defined as follows [42].

$$\delta_\nu\left(G_1, G_2\right)(j\omega) = \bar{\sigma}\left(\left(I + G_2 G_2^*\right)^{-1/2}\left(G_2 - G_1\right)\left(I + G_1^* G_1\right)^{-1/2}\right)(j\omega) \tag{30}$$

where $\bar{\sigma}(\cdot)$ denotes the maximum singular value, $(\cdot)^*$ represents conjugate transpose.

The ν-gaps between the high-fidelity model and the reduced-order models (46th-order and 19th-order respectively) for inputs and outputs of wingtip control surfaces and IMUs are shown in Fig. 4. In addition, the ν-gap between the 56th-order bottom-up model and the high-fidelity model is also provided for comparison. Comparing the results of the 46th-order model with those of the 56th-order bottom-up model indicates that integrating the aerodynamic-elastic model first and then applying the projection-based LPV model order reduction method allows for retaining fewer modes without increasing the ν-gap. When the model is reduced to the 19th-order, the ν-gap slightly increases, but near the critical flutter frequencies, its values are still far less than 1. This is because the dynamics of the aircraft in this frequency range are primarily dominated by the flutter modes, and the balanced truncation effectively preserves this characteristic of the system. From the comparison of pole migrations between the 19th-order and high-fidelity models in Fig. 5, it can be seen that, although the states of the model obtained through balanced truncation no longer have clear physical meaning, the pole trajectories associated with the two flutter modes remain highly consistent with those of the corresponding states in the original model.

https://doi.org/10.1017/aer.2025.41 Published online by Cambridge University Press

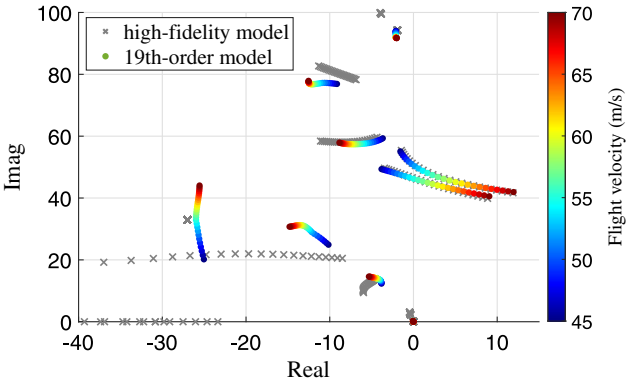


Figure 5. *Pole migrations of the high-fidelity model and the 19th-order model.*

4.2 Comparison of frequency domain responses

The comparison of the frequency domain responses between the high-fidelity model and reduced-order models at 54 m/s are shown in Figs 6 and 7. In the concerned frequency range, there is no significant difference between the 46th-order model and the 56th-order bottom-up model, both of which accurately reflect the input-output response of the high-fidelity model. The plots of the 19th-order model exhibit varying differences from the high-fidelity model across different input-output pairs and frequency ranges. These differences arise because the contributions of energy associated with different input-output channels to the system vary across different frequency bands, while balanced truncation tends to retain the components that significantly contribute to the system's energy. For instance, because the longitudinal position of the main wing's control surfaces are very close to the centre of gravity, their contributions to the pitch attitude are minimal. Consequently, the 19th-order model does not preserve the characteristics from WL4 to the pitch rate, leading to a notable difference in the corresponding Bode plot compared to the high-fidelity model, as shown in Fig 7. However, the low-frequency responses of the rigid-body attitude, as well as the wingtip vibration responses near the flutter frequencies, are effectively captured by the 19th-order model.

4.3 Comparison of time domain responses

To further verify the fidelity of the reduced-order models, open-loop time-domain simulations are also employed. Figure 8 shows the responses of both the high-fidelity and reduced-order models to the WL4 control surface doublet command at 48 m/s. At this speed, the aircraft exhibits static stability. The disturbance from the wingtip control surface induces large-amplitude flexible vibrations and small-amplitude rigid-body attitude motions, both of which gradually decay after the disturbance ends. Apart from the inability to accurately capture the ultra-high-frequency response at the wingtip caused by sudden signal changes, the reduced-order models are generally able to reflect the aircraft's dynamic response well. The bottom-up model shows smaller errors in pitch motion and speed variations, while the 46th-order and 19th-order models are more aligned with the high-fidelity model in terms of roll motion and wingtip vibrations.

Figure 9 illustrates the responses of different models to a step throttle increment at an initial speed of 51 m/s. The increase in throttle leads to a significant rise in the aircraft's speed, exceeding the first critical flutter speed of 52 m/s and approaching the second critical flutter speed of 55 m/s. During this process, the wingtip vibrations of the aircraft gradually increase and tend to diverge. All reduced-order models still adequately reflect the aircraft's dynamic response. However, the fidelity of the 19th-order and 46th-order models is obvious higher than that of the bottom-up model. Overall, the model order reduction approach described in this paper achieves a lower-order reduction compared to the bottom-up

https://doi.org/10.1017/aer.2025.41 Published online by Cambridge University Press

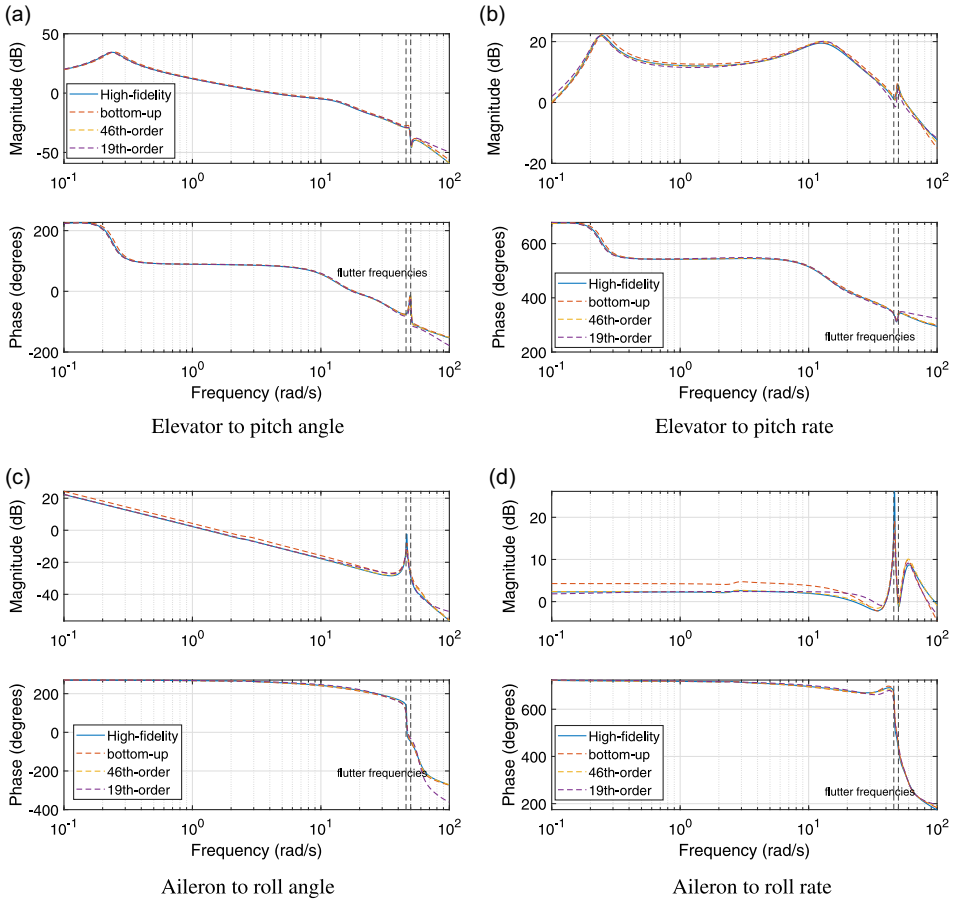


Figure 6. *Bode plots from the elevator and aileron to rigid-body motions.*

model while preserving the key dynamic characteristics of the high-fidelity model. The resulting 19th-order model can effectively represent the dynamic behaviour of the high-fidelity model and will be used for subsequent controller design.

5.0 LPV controller design

For flexible aircraft like FLEXOP, the controller needs to achieve both rigid body attitude control and flutter suppression. In the previous studies, the design approach separates the rigid body and flexible control. The rigid body control uses parameter-dependent proportional-integral-derivative control, while flutter control is divided into two types: one based on structured gain scheduling control [37], and the other on robust control [16, 17]. These methods extend the flutter boundaries of the aircraft to some extent, but they do not explicitly account for the effects of rigid-flexible coupling in the design synthesis. In practical applications, additional filters are necessary to prevent interactions between the baseline controller and the flutter suppression controller. Considering the close frequency of the two flutter modes and the increasing rigid-flexible coupling effects with velocity, this paper directly utilises robust control theory to design an LPV attitude and velocity tracking controller capable of maintaining the stability of flexible modes. The corresponding control problem is typically formulated as finding a parameter-dependent controller that ensures the stability of the closed-loop system and minimises the robust performance indices of the closed-loop system within the defined parameter range.

https://doi.org/10.1017/aer.2025.41 Published online by Cambridge University Press

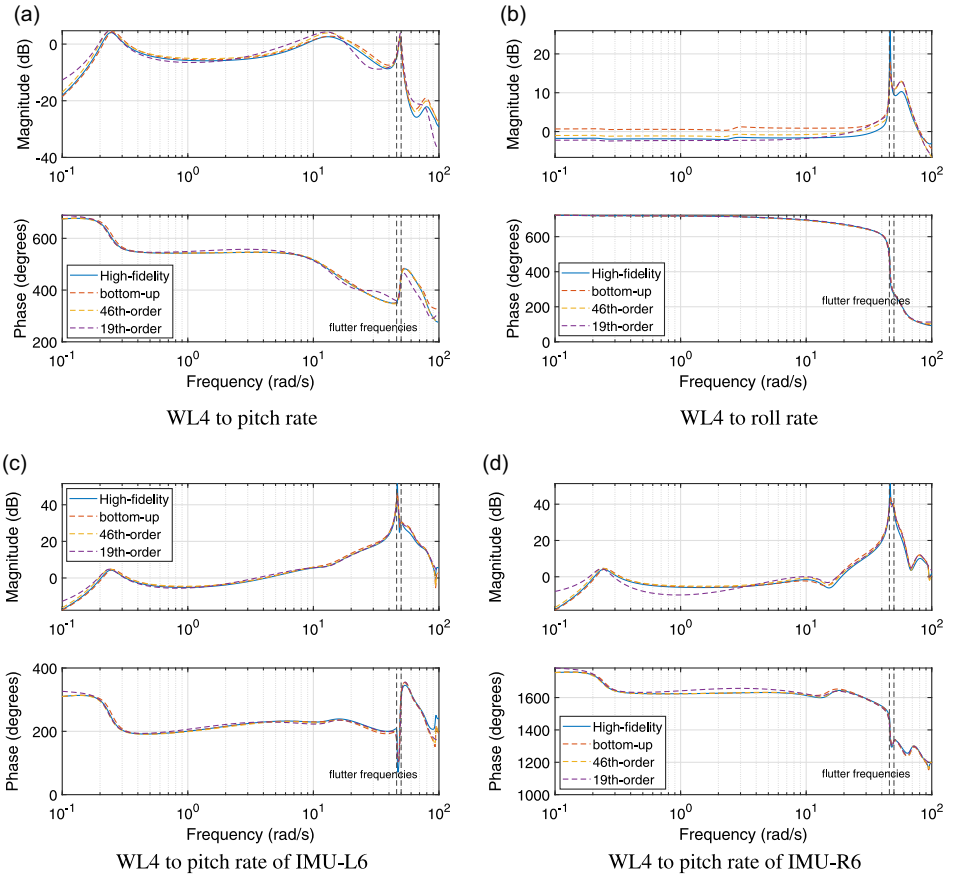


Figure 7. *Bode plots from the WL4 control surface to rigid-body and flexible motions.*

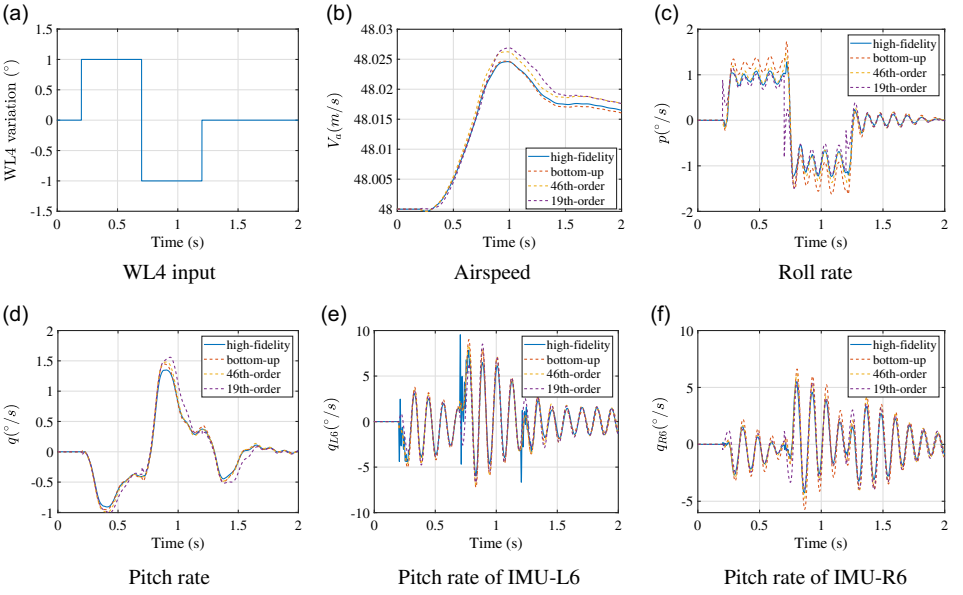


Figure 8. *Responses of different models to the doublet deflection of WL4 at 48 m/s.*

https://doi.org/10.1017/aer.2025.41 Published online by Cambridge University Press

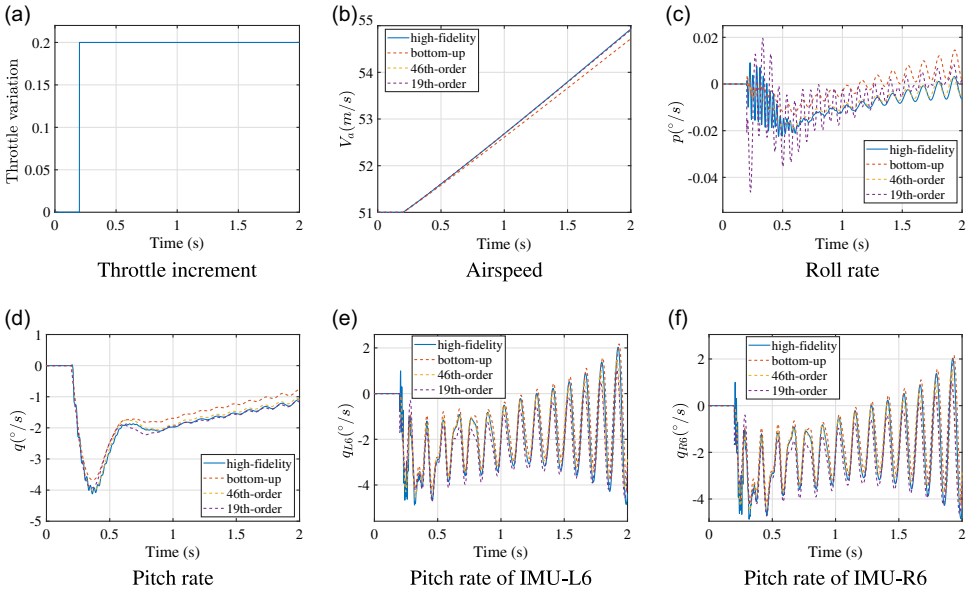


Figure 9. *Responses of different models to the step throttle increment at 51 m/s.*

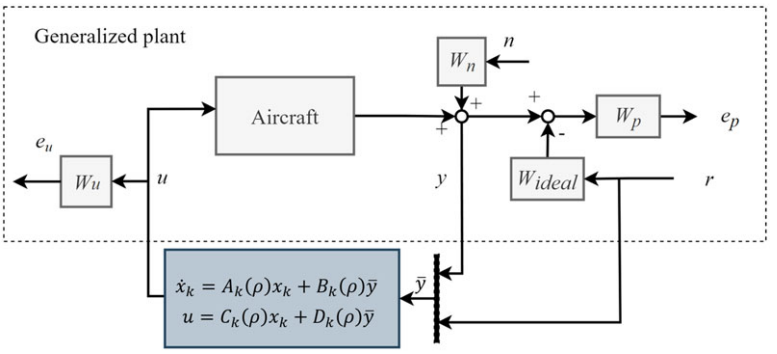


Figure 10. *Weighted interconnection of the closed-loop control system.*

5.1 Dynamic output feedback control design

Figure 10 shows the structure of the closed-loop weighted control system used for the design of the LPV dynamic output feedback controller. The reference $r = [r_{V_a}; r_\theta; r_\phi]$ contains target values of flight velocity, pitch angle and roll angle. The measurement output of the aircraft model is $y = [V_a, \theta, q, \phi, p, \beta, q_{l6}, q_{r6}]$. In addition to the signals that need to be tracked, it also includes pitch rate q, roll rate p, sideslip angle β, as well as pitch rates q_{l6} and q_{r6} from the IMU L6 and R6.

Selecting induced L_2 norm as the performance index, for the generalised plant depicted in Fig. 11, the problem of LPV dynamic output feedback controller can be defined as finding a parameter-dependent controller in the state-space representation, which can stabilise the closed-loop system and minimise induced L_2 gain from exogenous signals w to controlled outputs z. According to the result in literature [43], it can be formulated as a convex optimisation problem with linear matrix inequality constraints.

https://doi.org/10.1017/aer.2025.41 Published online by Cambridge University Press

Table 1. *Design of weighting or constraint coefficients*

Parameter	Target Performance	Weight Coefficient
Velocity	Tracking error $\lvert V_{ideal} - V_a \rvert < 0.1$ m/s	$W_{p,V_a} = 10$
Pitch angle	Tracking error $\lvert \theta_{ideal} - \theta \rvert < 0.72^\circ$	$W_{p,\theta} = 80$
Roll angle	Tracking error $\lvert \phi_{ideal} - \phi \rvert < 0.72^\circ$	$W_{p,\phi} = 80$
Control surfaces	Control surface command $\lvert \delta_{cs} \rvert < 0.5$	$W_{u,\delta_s} = 2$
Throttle	Throttle command $\lvert \delta_t \rvert < 1$	$W_{u,\delta_t} = 1$

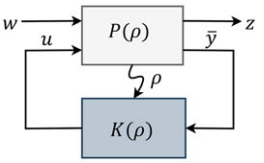


Figure 11. *General framework of LPV control system.*

In order to obtain the desired dynamic performance for reference tracking, an ideal model block W_{ideal} is introduced in Fig. 10 to generate the ideal response for the reference r.

$$\begin{aligned} W_{ideal} &= \text{diag}\left(W_{ideal,V_a}, W_{ideal,\theta}, W_{ideal,\phi}\right) \\ W_{ideal,V_a} &= \frac{0.81}{s^2+1.44s+0.81} \\ W_{ideal,\theta} &= \frac{2.25}{s^2+2.4s+2.25} \\ W_{ideal,\phi} &= \frac{2.25}{s^2+2.4s+2.25} \end{aligned} \tag{31}$$

where diag(·) denotes a diagonal block composed of diagonal elements specified inside the parentheses. The ideal models corresponding to each reference signal are defined as standard second-order systems. The weighting function W_p is used to limit the steady-state error between the ideal and actual responses and can be expressed as

$$W_p = \text{diag}\left(W_{p,V_a}, W_{p,\theta}, W_{p,\phi}\right) \tag{32}$$

where W_{p,V_a},$W_{p,\theta}$ and $W_{p,\phi}$ are designed based on the desired error responses of speed, pitch angle and roll angle, respectively. To avoid introducing excessive dynamic states, they are set as constants, as shown in Table 1. The weighting matrix W_u is used to limit the amplitude of controller outputs.

$$W_u = \text{diag}\left(W_{u,\delta_{cs}}, W_{u,\delta_{cs}}, W_{u,\delta_{cs}}, W_{u,\delta_t}\right) \tag{33}$$

Its diagonal components correspond sequentially to the ailerons, elevators, rudder and throttle, with specific values provided in Table 1. In addition, W_n is used to account for the influence of measurement noise and is defined as

$$W_n = \text{diag}\left(0.1, 0.01, 0.01, 0.01, 0.01, 0.01, 0.01, 0.01\right) \tag{34}$$

where the diagonal elements represent the amplitude of the noise, corresponding to the measurement signal y. By interconnecting the aircraft dynamic model and weighting functions in Fig. 10, the generalised plant $P(\rho)$ can be obtained. It can be represented by the following state-space model.

$$\begin{aligned} \dot{\bar{x}} &= \bar{A}(\rho)\,\bar{x} + \bar{B}_u(\rho)\,u + \bar{B}_w(\rho)\,w \\ z &= \bar{C}_z(\rho)\,\bar{x} + \bar{D}_{zu}(\rho)\,u + \bar{D}_{zw}(\rho)\,w \\ \bar{y} &= \bar{C}_y(\rho)\,\bar{x} + \bar{D}_{yu}(\rho)\,u + \bar{D}_{yw}(\rho)\,w \end{aligned} \tag{35}$$

where u represents the control input, $\bar{y} = \left[y;r\right]$ represents the generalised measurement output, $z = \left[e_u;e_p\right]$ represents the regulated output, and $w = [r;n]$ represents the external disturbance (including reference signals). Then, based on literature [43], the linear matrix inequalities can be formulated to solve for the parameter-dependent controller.

https://doi.org/10.1017/aer.2025.41 Published online by Cambridge University Press

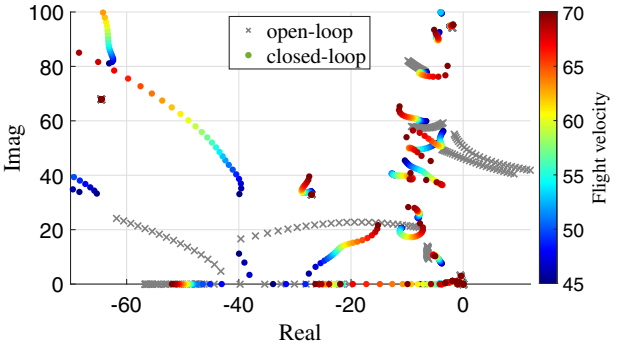


Figure 12. *Comparison of pole migrations of open-loop and closed-loop models.*

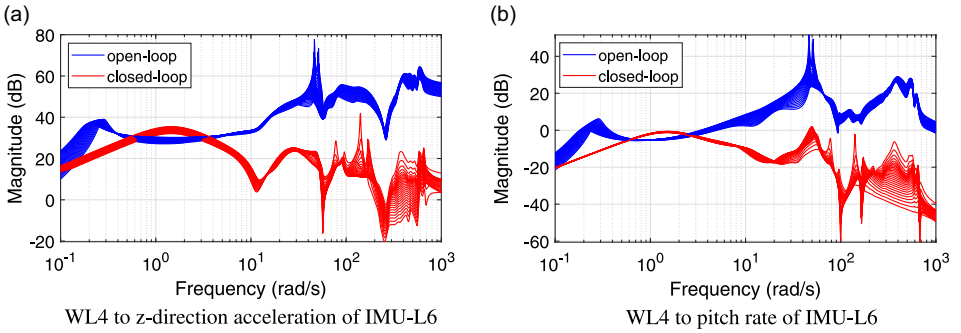


Figure 13. *Comparison of Bode plots between open-loop and closed-loop models.*

5.2 Results and discussions

By using the methods and parameter settings described in the previous subsection, a 25th-order controller is obtained based on the reduced-order model, with corresponding performance index γ of 1.20. Note that Algorithm 1 can also be used for order reduction of the LPV controller, which is further reduced to 21st-order. The derived controller has a fastest pole of 57.3 Hz, allowing it to be implemented on FLEXOP's onboard hardware (with a sampling frequency of 200 Hz).

5.2.1 Frequency domain analysis

The pole trajectories of the open-loop high-fidelity model and the closed-loop system formed by connecting this model with the 21st-order controller are shown in Fig. 12. It can be seen that, within the concerned speed and frequency ranges, under the influence of the designed controller, the flutter modes that originally become unstable with increasing velocity are stabilised, and other flexible as well as rigid modes also remain stable.

The open-loop and closed-loop frequency domain responses of the full-order model are shown in Fig. 13. The input is selected as WL4, and the outputs are chosen to be the z-direction acceleration and pitch rate from the IMU-L6 located at the left wingtip. The response magnitude of the closed-loop system shows a slight increase only in a small range around 1.5 rad/s (the design frequency of the ideal models). While in other frequency bands, especially near the flutter frequencies, the values are obvious lower than those of the open-loop system. This indicates that the disturbance from the wingtip control surface to the wingtip vibration will be significantly reduced, as the controller effectively increases the damping of the flutter modes.

To evaluate the robustness of the controller, the worst-case gain and phase margins of the closed-loop system at different flight velocities are presented in Fig.14. First, consider the margins of the individual loops. Due to the inherently large damping of the rigid-body motion modes and their control by multiple

https://doi.org/10.1017/aer.2025.41 Published online by Cambridge University Press

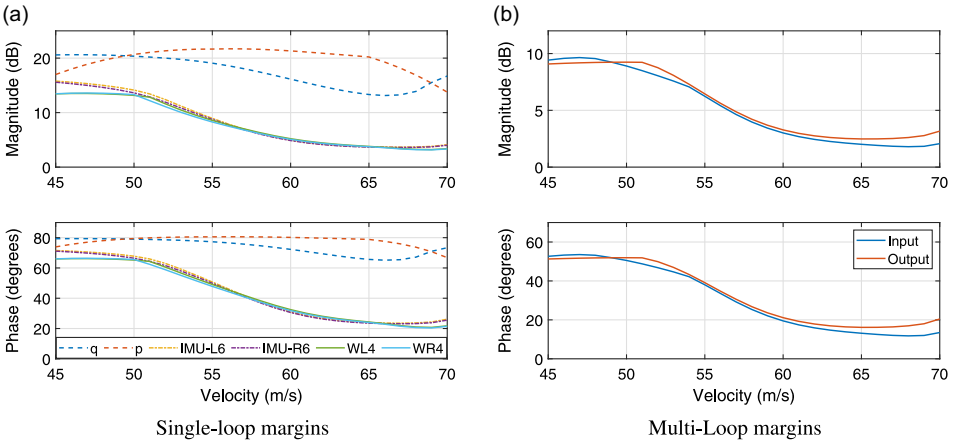


Figure 14. *Single-loop and multi-loop margins.*

control surfaces, the p and q loops clearly exhibit strong robustness, with minimal impact from flight velocity. The loop-at-a-time margins for the channels of outermost control surfaces and sensors are close in their value and gradually decrease as the flight velocity increases. Under the effect of the LPV controller, the rate of decline in loop-at-a-time margins with flight speed is much smoother compared to the damping decrease of the flutter modes of the aircraft. Even at a velocity close to 70 m/s, these loops still maintain a gain margin of approximately 5 dB and a phase margin of 20 degrees. Multi-loop margins address situations where multiple loops may have uncertainties or variations either individually or simultaneously, providing a more comprehensive robustness evaluation. In Fig.14(b), the inputs include the throttle and all control surface channels, while the outputs consist of all the sensor signals. Due to the mutual interactions between different loops, the margins associated with the multi-loop inputs and outputs are reduced compared to those of the individual loops. However, as a result of the integrated rigid-flexible coupling controller design, the closed-loop system is able to maintain a certain level of robustness within the designed velocity range.

5.2.2 Time domain analysis

To verify the attitude tracking performance of the controller, closed-loop simulations are conducted using the full-order high-fidelity LPV model. To better reflect engineering practice, Gaussian white noise has been added to the sensor measurement signals. Three velocity points, 48 m/s, 54 m/s and 65 m/s, are selected to demonstrate the capability of the designed controller in scenarios where the original model is stable, a single flutter mode is unstable and two flutter modes are unstable. The step responses of pitch angle tracking and roll angle tracking are given in Figs 15 and 16. With the parameter-dependent controller, while maintaining stability, the aircraft achieves great attitude tracking in accordance with the ideal response, with very small tracking errors and performance that is almost unaffected by changes in velocity. Due to the damping effect of the controller, the symmetric and anti-symmetric responses of both wingtips during pitch and roll tracking are primarily caused by rigid-body motion. The sudden change in commands only induces small wingtip vibrations, which quickly decay to near zero.

To validate the flutter suppression capability of the designed controller with continuous changes in scheduling parameter, velocity tracking simulations are performed within the design parameter range. Under steady-level flight at 45 m/s, a staircase command that increases by 5 m/s every 10 seconds is given. The aircraft's velocity, pitch rate, z-direction accelerations of the IMU-L6 and IMU-R6, and the control surface responses are illustrated in Fig. 17. The aircraft velocity closely tracks the ideal response, while the wingtip vibrations are maintained within a relatively small range. At each step of the command, very small-amplitude high-frequency oscillations can be observed, which are quickly

https://doi.org/10.1017/aer.2025.41 Published online by Cambridge University Press

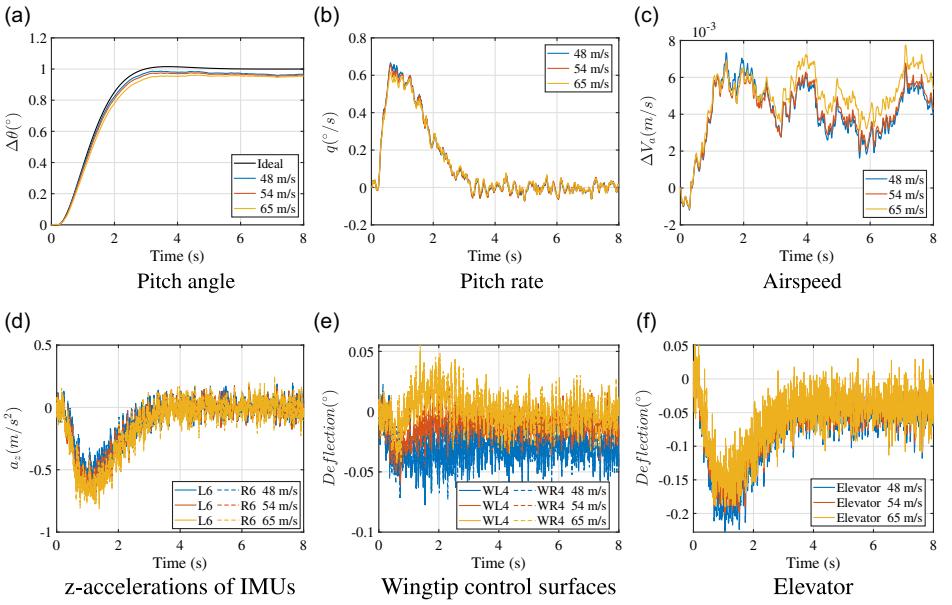


Figure 15. *Responses of pitch angle tracking under different velocities.*

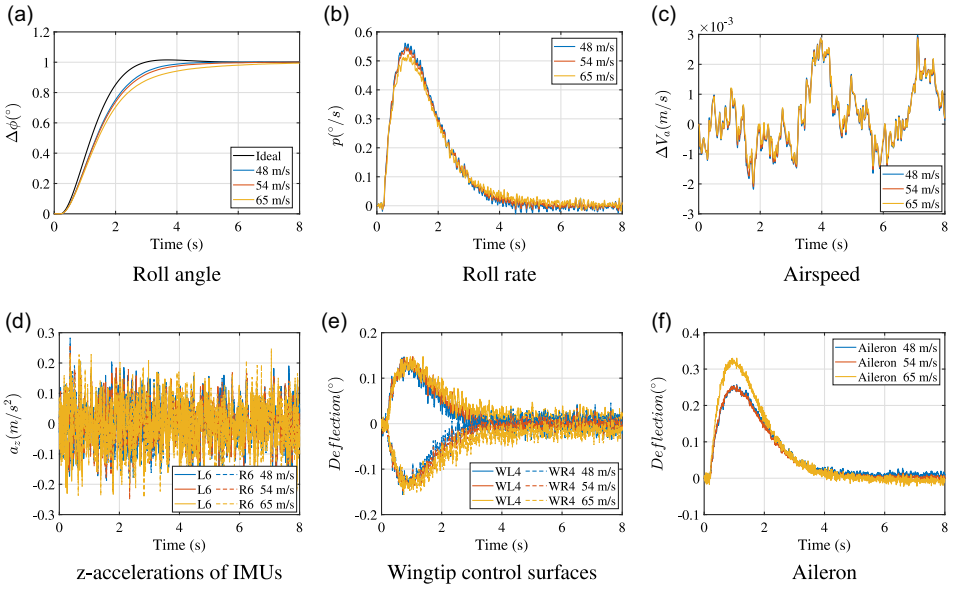


Figure 16. *Responses of roll angle tracking under different velocities.*

dissipated. Compared to the open-loop simulations shown in Fig. 9, the aircraft is able to smoothly pass through the critical flutter speeds under the damping effect of the controller. Due to the low-order model's omission of the high-frequency characteristics of the high-fidelity model, although the predicted stability range of the original two flutter modes is extended to over 70 m/s, the aircraft experiences extremely high-frequency oscillations that tend to diverge when the airspeed exceeds 68 m/s. However, compared to the critical flutter speeds of 61 m/s and 63 m/s reported in the literatures [16, 17], the flutter-free flight envelope of the aircraft has experienced a noticeable improvement. Although retaining more high-frequency modes during the model order reduction process can further mitigate the effects

https://doi.org/10.1017/aer.2025.41 Published online by Cambridge University Press

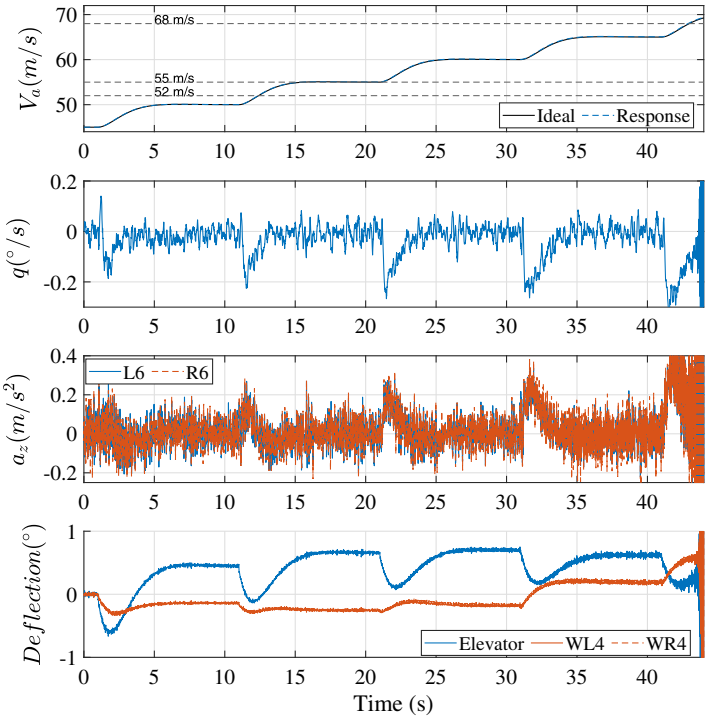


Figure 17. *Responses during velocity tracking.*

of high-frequency distortion, but it also increases the controller's frequency, making it impractical for engineering implementation. The controller designed in this paper achieves a good balance between performance and practical applicability.

6.0 Conclusions

This paper presents a detailed derivation and implementation process of the projection-based LPV model order reduction method. The state consistency of the reduced-order model obtained through this method can be ensured, and modal truncation and balanced truncation of the LPV model can be achieved by constructing reduction transformation matrices using different approaches. Utilising the proposed method, the high-fidelity model of the FLEXOP aircraft is sequentially reduced to 46th-order and then to 19th-order. The fidelity of the reduced models is validated by comparing their responses with those of the full-order model in both frequency domain and time domain. Compared to the previous bottom-up modeling approach, this method significantly reduces the order of the FLEXOP aircraft while preserving key dynamic characteristics and avoids the trial-and-error process of selecting retained states across different subsystems. Based on the obtained 19th-order model, a parameter-dependent dynamic output feedback controller is designed. The designed controller effectively handles attitude tracking for the full-order model while maintaining consistent performance across different parameter values. Under conditions of continuous flight speed variation, the controller successfully stabilises the flutter modes and keeps the aicraft's flexible vibrations within a small range. Compared to previously published research, this method demonstrates more effective expansion of the flight speed envelope of the FLEXOP.

Acknowledgements. The authors would like to express our gratitude to Bálint Vanek for providing the model and to the FLEXOP project team for their contributions.

Competing interests. The author(s) declare none.

https://doi.org/10.1017/aer.2025.41 Published online by Cambridge University Press

References

[1] Baharozu, E., Soykan, G. and Ozerdem, M.B. Future aircraft concept in terms of energy efficiency and environmental factors, *Energy*, 2017, **140**, pp 1368–1377.

[2] Khalil, A. and Fezans, N. Gust load alleviation for flexible aircraft using discrete-time h_{∞}h∞ preview control, *Aeronaut. J.*, 2021, **125**, (1284), pp 341–364.

[3] Saporito, M., Da Ronch, A., Bartoli, N. and Defoort, S. Robust multidisciplinary analysis and optimization for conceptual design of flexible aircraft under dynamic aeroelastic constraints, *Aerosp. Sci. Technol.*, 2023, **138**, p 108349.

[4] Burnett, E.L., Beranek, J.A., Holm-Hansen, B.T., Atkinson, C.J. and Flick, P.M. Design and flight test of active flutter suppression on the X-56A multi-utility technology test-bed aircraft, *Aeronaut. J.*, 2016, **120**, (1228), pp 893–909.

[5] Hiller, B.R., Frink, N.T., Silva, W.A. and Mavris, D.N. Aeroelastic indicial response reduced-order modeling for flexible flight vehicles, *J. Aircr.*, 2020, **57**, (3), pp 469–490.

[6] Meddaikar, Y.M., Dillinger, J., Klimmek, T., et al. Aircraft aeroservoelastic modelling of the FLEXOP unmanned flying demonstrator, *AIAA Scitech 2019 Forum*, San Diego, CA, USA, AIAA, 2019, p 1815.

[7] Kier, T.M. Comparing different potential flow methods for unsteady aerodynamic modelling of a flutter demonstrator aircraft, *AIAA SCITECH 2023 Forum*, National Harbor, MD, USA and Online, AIAA, 2023.

[8] Chu, L., Li, Q., Gu, F., Du, X., He, Y. and Deng, Y. Design, modeling, and control of morphing aircraft: a review, *Chin. J. Aeronaut.*, 2022, **35**, (5), pp 220–246.

[9] Meirovitch, L. and Tuzcu, I. Unified theory for the dynamics and control of maneuvering flexible aircraft, *AIAA J.*, 2004, **42**, (4), pp 714–727.

[10] Waszak, M.R. and Schmidt, D.K. Flight dynamics of aeroelastic vehicles, *J. Aircr.*, 1988, **25**, (6), pp 563–571.

[11] Sharqi, B. and Cesnik, C.E.S. Finite element model updating for very flexible wings, *J. Aircr.*, 2023, **60**, (2), pp 476–489.

[12] He, T. and Su, W. Robust control of gust-induced vibration of highly flexible aircraft, *Aerosp. Sci. Technol.*, 2023, **143**, p 108703.

[13] Al-Jiboory, A.K., Zhu, G., Swei, S.S.-M., Su, W. and Nguyen, N.T. LPV modeling of a flexible wing aircraft using modal alignment and adaptive gridding methods, *Aerosp. Sci. Technol.*, 2017, **66**, pp 92–102.

[14] Luspay, T., Péni, T., Gőzse, I., Szabó, Z. and Vanek, B. Model reduction for LPV systems based on approximate modal decomposition, *Int. J. Numer. Methods Eng.*, 2018, **113**, (6), pp 891–909.

[15] Takarics, B., Vanek, B., Kotikalpudi, A. and Seiler, P. Flight control oriented bottom-up nonlinear modeling of aeroelastic vehicles, *2018 IEEE Aerospace Conference*, Big Sky, MT, USA, IEEE, 2018, pp 1–10.

[16] Patartics, B., Lipták, G., Luspay, T., Seiler, P., Takarics, B. and Vanek, B. Application of structured robust synthesis for flexible aircraft flutter suppression, *IEEE Trans. Control Syst. Technol.*, 2022, **30**, (1), pp 311–325.

[17] Takarics, B. and Vanek, B. Robust control design for the flexop demonstrator aircraft via tensor product models, *Asian J. Control*, 2021, **23**, (3), pp 1290–1300.

[18] Roessler, C., Bartasevicius, J., Koeberle, S.J., et al. Results of an aeroelastically tailored wing on the FLEXOP demonstrator aircraft, *AIAA Scitech 2020 Forum*, Orlando, FL, USA, AIAA, 2020. https://doi.org/10.2514/6.2020-1969

[19] Theis, J., Takarics, B., Pfifer, H., Balas, G.J. and Werner, H. Modal matching for LPV model reduction of aeroservoelastic vehicles, *AIAA Atmospheric Flight Mechanics Conference*, Kissimmee, FL, USA, AIAA, 2015. https://doi.org/10.2514/6.2015-1686

[20] Moreno, C., Seiler, P. and Balas, G. Linear, parameter varying model reduction for aeroservoelastic systems, *AIAA Atmospheric Flight Mechanics Conference*, Minneapolis, MN, USA, AIAA, 2012. https://doi.org/10.2514/6.2012-4859

[21] Wood, G.D. *Control of Parameter-Dependent Mechanical Systems*, PhD thesis, University of Cambridge, 1995.

[22] Zhang, Q. and Ljung, L. LPV system common state basis estimation from independent local LTI models, *IFAC-PapersOnLine*, 2015, **48**, (28), pp 190–195.

[23] Theis, J., Seiler, P. and Werner, H. LPV model order reduction by parameter-varying oblique projection, *IEEE Trans. Control Syst. Technol.*, 2017, **26**, (3), pp 773–784.

[24] Zhu, J., Wang, Y., Pant, K., Suh, P.M. and Brenner, M.J. Genetic algorithm-based model order reduction of aeroservoelastic systems with consistent states, *J. Aircr.*, 2017, **54**, (4), pp 1443–1453.

[25] Liu, Y., Gao, W., Li, Q. and Lu, B. Oblique projection-based modal matching algorithm for LPV model order reduction of aeroservoelastic systems, *Aerospace*, 2023, **10**, (5), p 406.

[26] Liu, Y., Niu, X., Li, Q. and Lu, B. An improved linear parameter-varying modeling, model order reduction, and control design process for flexible aircraft, *Aerosp. Sci. Technol.*, 2024, **144**, p 108765.

[27] Fournier, H., Massioni, P., Tu Pham, M., Bako, L., Vernay, R. and Colombo, M. Robust gust load alleviation of flexible aircraft equipped with Lidar, *J. Guid. Control Dyn.*, 2022, **45**, (1), pp 58–72.

[28] Wang, X., Van Kampen, E., Chu, Q.P. and De Breuker, R. Flexible aircraft gust load alleviation with incremental nonlinear dynamic inversion, *J. Guid. Control Dyn.*, 2019, **42**, (7), pp 1519–1536.

[29] Wang, Y., Wynn, A. and Palacios, R. Model-Predictive control of flexible aircraft dynamics using nonlinear reduced-order models, *57th AIAA/ASCE/AHS/ASC Structures, Structural Dynamics, and Materials Conference*, San Diego, California, USA, AIAA, 2016. https://doi.org/10.2514/6.2016-0711

[30] Wagner, D., Henrion, D., and Hromčík, M. Advanced algorithms for verification and validation of flexible aircraft with adaptive control, *J. Guid. Control Dyn.*, 2023, **46**, (3), pp 600–607.

[31] Wang, X., Mkhoyan, T. and De Breuker, R. Nonlinear incremental control for flexible aircraft trajectory tracking and load alleviation, *J. Guid. Control Dyn.*, 2022, **45**, (1), pp 39–57.

[32] Zeng, J., Moulin, B., De Callafon, R. and Brenner, M.J. Adaptive feedforward control for gust load alleviation, *J. Guid. Control Dyn.*, 2010, **33**, (3), pp 862–872.

https://doi.org/10.1017/aer.2025.41 Published online by Cambridge University Press

[33] White, A.P., Zhu, G. and Choi, J. *Linear Parameter-Varying Control for Engineering Applications*, Springer, Berlin, German, 2013.
[34] Barker, J.M. and Balas, G.J. Comparing linear parameter-varying gain-scheduled control techniques for active flutter suppression, *J. Guid. Control Dyn.*, 2012, **23**, (5), 948–955.
[35] Pfifer, H., Moreno, C.P., Theis, J., Kotikapuldi, A., Gupta, A., Takarics, B. and Seiler, P. Linear parameter varying techniques applied to aeroservoelastic aircraft: In memory of Gary Balas, *IFAC-PapersOnLine*, 2015, **48**, (26), pp 103–108.
[36] Hjartarson, A., Seiler, P.J., Packard, A. and Balas, G.J. LPV aeroservoelastic control using the LPV tools toolbox, *AIAA Atmospheric Flight Mechanics (AFM) Conference*, Boston, MA, USA, AIAA, 2013, p 4742.
[37] Pusch, M., Ossmann, D. and Luspay, T. Structured control design for a highly flexible flutter demonstrator, *Aerospace*, 2019, **6**(3), p 27.
[38] Villemagne, C.D. and Skelton, R.E. Model reductions using a projection formulation, *26th IEEE Conference on Decision and Control*, Los Angeles, CA, USA, IEEE, 1987, 26, pp 461–466.
[39] Benner, P., Grivet-Talocia, S., Quarteroni, A., Rozza, G., Schilders, W. and Silveira, L. *Model Order Reduction: Volume 1: System-And Data-Driven Methods and Algorithms*, De Gruyter, Berlin, German, 2021, pp 17–18.
[40] Moore, B. Principal component analysis in linear systems: controllability, observability, and model reduction, *IEEE Trans. Automat. Control*, 1981, **26**, (1), pp 17–32.
[41] Brunton, S.L. and Kutz, J.N. *Data-Driven Science and Engineering: Machine Learning, Dynamical Systems, and Control*, Cambridge University Press, Cambridge, UK, 2019.
[42] Vinnicombe, G. *Uncertainty and Feedback: H infinity Loop-Shaping and the nu-gap Metric. G – Reference, Information and Interdisciplinary Subjects Series*, Imperial College Press, London, UK, 2001.
[43] Apkarian, P. and Adams, R. Advanced gain-scheduling techniques for uncertain systems, *IEEE Trans. Control Syst. Technol.*, 1998, **6**, (1), pp 21–32.

Cite this article: Gao W., Jiang W., Li Q. and Lu B. (2025). Linear parameter-varying model order reduction and control design of FLEXOP demonstrator aircraft. *The Aeronautical Journal*, **129**, 2648–2669. https://doi.org/10.1017/aer.2025.41

https://doi.org/10.1017/aer.2025.41 Published online by Cambridge University Press